Atmos. Meas. Tech. Discuss., 4, 1493–1531, 2011
www.atmos-meas-tech-discuss.net/4/1493/2011/
doi:10.5194/amtd-4-1493-2011

Atmospheric Measurement Techniques Discussions

On cloud ice induced absorption and polarisation effects in microwave limb sounding

P. Eriksson and B. Rydberg

Department of Earth and Space Sciences, Chalmers University of Technology, Gothenburg, Sweden

Received: 8 February 2011 – Accepted: 20 February 2011 – Published: 2 March 2011

Correspondence to: P. Eriksson (patrick.eriksson@chalmers.se)

Published by Copernicus Publications on behalf of the European Geosciences Union.

Abstract

Detailed simulations of microwave limb sounding in the presence of ice clouds have been performed. It is clarified that, while particle absorption normally gives no significant change of the measured radiance for down-looking measurements, this is not the case for limb sounding. The particles were treated as horizontally aligned oblate spheroids and for this assumption on particle shape, and comparable situations, no significant degree of circular polarisation is generated. Differences between the brightness temperature of the ±45° polarisation components up to 4 K were found, but this difference appears to be small as long as single scattering conditions apply. The cloud extinction is the smallest for the vertically polarised component, but it should be more beneficial to observe any of the ±45° and circularly polarised components if ice water content is also a target of the retrievals. These latter pairs of orthogonal components also make it easier to combine information measured from different positions and with different polarisations. The results indicate that single scattering can be assumed for cloud optical thicknesses below about 0.1, which is thus an important threshold with respect to the complexity and accuracy of retrievals. The representation of particle sizes during the retrieval is discussed.

1 Introduction

The bulk of data provided so far by limb sounding sensors covers the stratosphere and the lower mesosphere, but both scientific objectives and the technical development move the emphasis towards the upper troposphere (UT). For example, the PREMIER mission proposal (ESA, 2008) is a manifestation of this change in scientific focus. Any satellite observation into the troposphere must deal with the impact of clouds, and this aspect is of special importance for limb sounding due to the long horizontal path lengths. In this respect, microwave techniques have an inherent advantage as the

AMTD
4, 1493–1531, 2011

sensitivity to clouds is significantly lower at these long wavelengths, compared to the infrared and optical regions (e.g. Ekström et al., 2008).

In fact, a large fraction of microwave limb sounding data can be handled as "clear sky". The size of this fraction depends on the wavelengths used and the local atmospheric conditions. In any case, cloud effects should be considered as this decreases the uncertainties of the gas species retrievals and increases the data yield. However, the treatment of clouds in microwave limb sounding gas inversion algorithms is highly simplified. Clouds are in best case partly considered by a general continuum absorption term. Such a term is applied in the Odin-SMR (Murtagh et al., 2002) and Aura MLS (Waters et al., 2006) inversions (Urban et al., 2005; Livesey et al., 2006), and is introduced primarily to handle uncertainties in absorption originating from non-local transitions and poorly understood physical mechanisms (see Rosenkranz, 1993). This term would also cover the impact of clouds if they could be treated as purely absorbing matter.

A more elaborated inclusion of clouds, taking full account of scattering, is found in the methodology of Rydberg et al. (2009). Water vapour and cloud ice water content (IWC) are retrieved in parallel from Odin-SMR data, but only spectra from single tangent altitudes are used and there is no obvious way to extend the approach to invert complete limb sounding sequences.

The interaction between microwave radiation and clouds is quite well studied for frequencies below 100 GHz and ground-based or down-looking observation geometries (a review is given by Battaglia et al., 2006). The situation is quite different for the frequencies (>150 GHz) and incidence angles ($\approx 90^{\circ}$) under consideration here, and the basic justification of this study is that the development of more appropriate retrieval schemes requires a better understanding of how clouds affect microwave limb sounding radiances. The poorer knowledge for limb sounding could earlier be explained by a lack of relevant tools and input for the required simulations, but the situation has improved. Rigorous simulations of limb sounding measurements involving cloud scattering can now be performed by the ARTS software (Emde et al., 2004a; Davis et al., 2005a), and

AMTD
4, 1493–1531, 2011

since 2006 the CloudSat 94 GHz radar (Stephens et al., 2002) provides global information on cloud structures in a sufficient detailed manner. ARTS and CloudSat are key components of the study.

For this study, the altitude region of interest is the UT and focus is put on wavelengths around 1 mm (300 GHz). The term "mm" is used below in favour of "microwaves" to make a clear distinction to the range < 100 GHz. The analysis is made primarily from the perspective of trace gas retrievals. The primary frequency range for such retrievals inside the UT is 150–700 GHz (as indicated by the mm bands of Aura MLS). These observations can further provide information on IWC (Wu et al., 2005; Li et al., 2005; Eriksson et al., 2010b) and this aspect is also considered.

Upper tropospheric clouds consist mainly of ice particles, and only this type of clouds is considered here. It has been established that scattering is in general the dominating process for ice clouds at mm wavelengths (e.g. Evans and Stephens, 1995b; Emde et al., 2004b). The relative importance of absorption is higher for small particles (Evans and Stephens, 1995a; Wu et al., 2005) and with a cold radiative background (Eriksson et al., 2008, and Sect. 3). These conditions are of special concern for limb sounding and ice particle absorption should be more prominent for this measurement technique, but this issue has not yet been studied in any detail.

Polarisation effects are of special importance for microwave sensors as these devices are polarisation sensitive. There are three main options for the response, in fact all covered by the last three mm limb sounders: Odin-SMR detects the +45° and −45° linearly polarised components (Eriksson et al., 2007), Aura MLS measures the horizontal (H) and vertical (V) linear components (Wu et al., 2006) and SMILES (Kikuchi et al., 2010) observes the left- and right-hand circular components (Kasai, Y., personal communication, 2010).

Even spherical particles cause some difference between the V and H components for mm limb sounding (Teichmann et al., 2006). Several studies have shown that this difference increases with the aspect ratio of the particles, on the condition that a preferred orientation exists. However, these studies have either been performed for

AMTD
4, 1493–1531, 2011

a plane-parallel atmosphere (Czekala, 1998; Miao et al., 2003), down-looking geometry (Davis et al., 2007), for completely homogeneous (1-D) clouds (Davis et al., 2005b; Eriksson et al., 2007) or just a single synthetic cloud (Emde et al., 2004a; Davis et al., 2005a,b). In addition, there exists no investigation of the other polarisation components with a limb sounding focus.

The objectives of this work are, that for mm limb sounding: (1) Study the relative importance of ice particle absorption, (2) Calculate the complete polarisation state for a set of realistic scenarios, and, (3) Analyse the significance of the results for the retrievals.

2 Theory, tools and data

2.1 Radiative transfer

The intensity and polarisation state of radiation are described by the Stokes vector, $\boldsymbol{I}$. The radiative transfer equation to be solved in the case of thermal emission and particle scattering is

$$\frac{\mathrm{d}\boldsymbol{I}(\nu,\boldsymbol{r},\hat{\boldsymbol{n}})}{\mathrm{d}s} = -\mathbf{K}(\nu,\boldsymbol{r},\hat{\boldsymbol{n}})\boldsymbol{I}(\nu,\boldsymbol{r},\hat{\boldsymbol{n}}) + \boldsymbol{a}(\nu,\boldsymbol{r},\hat{\boldsymbol{n}})B(\nu,\boldsymbol{r}) + \int_{4\pi}\mathbf{Z}(\nu,\boldsymbol{r},\hat{\boldsymbol{n}},\hat{\boldsymbol{n}}')\boldsymbol{I}(\nu,\boldsymbol{r},\hat{\boldsymbol{n}}')\mathrm{d}\hat{\boldsymbol{n}}', \quad (1)$$

where ν is the frequency, $\boldsymbol{r}$ is the atmospheric position, $\hat{\boldsymbol{n}}$ is the propagation direction, s is the distance along $\hat{\boldsymbol{n}}$, $\mathbf{K}$ is the extinction matrix, $\boldsymbol{a}$ is the absorption vector, B is the Planck function and $\mathbf{Z}$ is the scattering matrix. See Mishchenko et al. (2002) for details regarding the assumptions for this equation and definitions of the involved quantities. $\mathbf{Z}$ is frequently denoted as the phase matrix, but scattering matrix (e.g. Bohren and Huffman, 1998) is clearly a more descriptive name.

During the actual calculations the vector $\boldsymbol{I}$ holds radiance values. For the presentation, simulated radiances are converted to Planck brightness temperatures following

AMTD
4, 1493–1531, 2011

the expressions in Eriksson et al. (2010a). The standard nomenclature of denoting the four elements of $\boldsymbol{I}$ as $I = [I,Q,U,V]^T$ is kept (Chandrasekhar, 1950), but they are here reported as

$$I = (T_B^v + T_B^h)/2, \quad (2)$$

$$Q = T_B^v - T_B^h, \quad (3)$$

$$U = T_B^{+45^\circ} - T_B^{-45^\circ}, \quad (4)$$

$$V = T_B^{\mathrm{lhc}} - T_B^{\mathrm{rhc}}, \quad (5)$$

where T_B^v is the brightness temperature [K] for the vertically linearly polarised component, calibrated with respect to the single polarisation power of blackbody radiation. T_B^h, $T_B^{+45^\circ}$, $T_B^{-45^\circ}$, T_B^{lhc} and T_B^{rhc} are defined likewise, but consider the horizontal linear, $+45^\circ$ linear, -45° linear, left-hand circular, and right-hand circular component, respectively. The element I could likewise be defined as the average of the other two pairs of orthogonal components ($T_B^{+45^\circ}/T_B^{-45^\circ}$ and $T_B^{\mathrm{lhc}}/T_B^{\mathrm{rhc}}$).

For clear-sky conditions, and as long as the tangent altitude is above the surface, the measured Stokes vector can be written as $I = [I_{cs},0,0,0]^T$. The impact of clouds is below reported as the difference to the corresponding case with all clouds removed from the simulations (i.e. clear-sky). Any difference for Q, U and V originates from the clouds and no further notation is needed. The difference for the first Stokes component is reported as ΔI:

$$\Delta I = I - I_{cs}, \quad (6)$$

where I and I_{cs} are the simulation result for complete atmosphere and corresponding clear-sky case, respectively.

The scattering of a particle is highly dependent on the ratio between its "characteristic size", d and the wavelength, λ, normally reported as the size parameter, x:

$$x = \frac{\pi d}{\lambda}. \quad (7)$$

AMTD
4, 1493–1531, 2011

That is, x is the ratio between circumference and wavelength for spherical particles.

2.2 Simulation software

The simulations were performed by ARTS (Atmospheric Radiative Transfer Simulator), a freely available, open source, software package (Buehler et al., 2005). The second version of ARTS (Eriksson et al., 2010a) includes two modules for solving Eq. (1). The Monte Carlo (MC) algorithm (Davis et al., 2005a) is used for this study. ARTS-MC allows simulation of cloud scattering in a three dimensional (3-D) atmosphere with arbitrary geoid and surface shapes, taking full account of polarisation effects. Gaseous absorption is calculated internally by ARTS, for efficiency reasons pre-calculated as a look-up table (Buehler and Eriksson, 2010). Particle optical (single scattering) properties are obtained through the T-matrix code by Mishchenko et al. (2002).

2.3 Atmospheric scenarios

An assumption of completely homogeneous cloud layers leads to a misrepresentation of cloud effects (Emde et al., 2004a; Davis et al., 2005a, 2007; Eriksson et al., 2007; Adams et al., 2008). Data on both horizontal and vertical cloud structures are obtained by high frequency cloud radars. CloudSat is the only satellite-based radar of this kind, and is selected in order to obtain large geographical coverage.

A methodology to make use of radar observations for simulating cloud effects in passive mm-wave data was developed by Rydberg et al. (2007), later extended to 3-D in order to create a database for Odin-SMR upper tropospheric water retrievals (Rydberg et al., 2009). This study makes use of the atmospheric scenarios generated for the Odin-SMR database. In short, along-track cross-sections of radar back-scattering, from CloudSat, is transformed to 3-D fields using the algorithm by Venema et al. (2006). The 3-D fields obtained are converted to fields of number densities using the particle size distribution (PSD) parametrisation by McFarquhar and Heymsfield (1997, below MH97). No retrievals are involved and final data are fully consistent with the basic

AMTD
4, 1493–1531, 2011

observations of CloudSat (see further Sect. 2.4). The database covers only tropical conditions (latitudes of ±30°).

In Rydberg et al. (2009) it is shown that these atmospheric scenarios result in simulations that reproduce in detail Odin-SMR observations. This indicates that cloud structures above 10 km and over horizontal distances below ∼ 40 km (the footprint size of the satellite data considered) are reasonably treated. To what extent the 3-D distribution of temperature and gas species is correctly captured is not known, where relationships between cloudy regions and surrounding air are especially uncertain, but in this context these aspects are secondary to the representation of clouds.

2.4 Simulation details

This work is part of a design study of the mm-wave limb sounder instrument for the PREMIER mission, and the frequency for the simulations is selected accordingly: 347.5 GHz. This is a frequency in-between transitions of e.g. CO and HCN (at 345.8 and 354.5 GHz, respectively), lacking local spectral features. The frequency 347.5 GHz corresponds roughly to the lowest opacity with respect to gaseous absorption for the instrument and can be treated as a "window frequency".

The absorption for water, oxygen and nitrogen is taken from Rosenkranz (1998), Rosenkranz (1993), and Liebe et al. (1993), respectively. To this is added the absorption of roughly 70 transitions of other species. Figure 1 summarises the average clear-sky radiative properties at 347.5 GHz. The opacity at this wavelength of 0.86 mm is roughly halfway between the one at 230 GHz and the one at 501/645 GHz the "window" frequencies of Aura MLS and Odin-SMR/SMILES, respectively.

The surface was assumed to have a spherical shape and to act as a blackbody. Monochromatic pencil beam simulations were performed for tangent altitudes of 4, 12, 14 and 16 km, with refraction neglected. The basic properties of results for 14 and 16 km are the same, and only results for 14 km are shown.

No liquid clouds are included. The shape of cloud ice particles is throughout (solid) oblate spheroids. The larger dimension of the particles is placed in the horizontal plane.

AMTD
4, 1493–1531, 2011

Two aspect ratios are considered: 1.2 and 2.0. The first value is taken from estimates obtained from parallel V and H Aura MLS 122 GHz data (Davis et al., 2005b). The second value is motivated by the fact that cirrus cloud particles are known to occasionally have very high aspect ratios, and be oriented as assumed here (e.g. Okamoto et al., 2010).

The original data from Rydberg et al. (2009) assume spherical particles. The complete particle size distribution is represented by 10 discrete sizes. The number density fields corresponding to each particle size are kept constant. The descriptive size for the modified aspect ratios is set in such way that the particle volume is kept constant; the IWC [gm^{-3}] is the same independently of aspect ratio. This approach is not maintaining a constant radar backscattering, and the perfect matching with the CloudSat observations (Sect. 2.3) is lost, but was judged to be the best alternative for the interpretation of the results.

3 Absorption vs. scattering

Focus in this section is on the first Stokes element (I) and expressions considering just this element are used. This is denoted as "scalar radiative transfer". These simplified expressions are also better suited for explaining the results.

3.1 Scalar radiative transfer

If polarisation effects can be neglected, the radiative transfer over a short part of the propagation path, extending between points i and $i+1$, can be approximated as

$$I^{i+1} = I^i e^{-kl} + (1 - e^{-kl})[(1 - \varpi)B + \varpi S], \quad (8)$$

where I^i is the intensity (for $\hat{\boldsymbol{n}}$) at point i, l is the distance along the path between i and $i+1$, k is the extinction coefficient (scalar correspondence to $\mathbf{K}$), ϖ is the single

AMTD
4, 1493–1531, 2011

scattering albedo and S can be seen as the source function for scattering. The last two quantities are defined as

$$\omega = \frac{k-a}{k} = \frac{s}{k}, \tag{9}$$

where a (scalar correspondence to $\boldsymbol{a}$) and s are the absorption and scattering coefficients, respectively, and

$$S = \int_{4\pi} p(\hat{\boldsymbol{n}}, \hat{\boldsymbol{n}}') \boldsymbol{I}(\hat{\boldsymbol{n}}') \mathrm{d}\hat{\boldsymbol{n}}', \tag{10}$$

where p is the normalised (otherwise scalar correspondence to $\mathbf{Z}$) scattering function:

$$\int_{4\pi} p(\hat{\boldsymbol{n}}, \hat{\boldsymbol{n}}') \mathrm{d}\hat{\boldsymbol{n}}' = 1. \tag{11}$$

3.2 Extinction

The extinction has two terms, absorption and scattering out of the line-of-sight. The relative size of the two terms is normally reported as the single scattering albedo (Eq. 9). Examples are found in Fig. 2. The single scattering albedo for spherical particles depends on two quantities, the size parameter and the complex refractive index ($n = n' + in''$). The real part of the refractive index of ice, n', is ≈ 1.8 throughout the microwave region and the imaginary part, n'', increases in a smooth manner from 0.001 around 80 GHz to 0.01 around 700 GHz (Warren and Brandt, 2008).

The data in Fig. 2 correspond to size parameters between 0.04 and 3.7, and Rayleigh ($x \ll 1$) and Mie ($x \approx 1$) conditions apply. For the Rayleigh regime, the absorption and scattering cross-sections are proportional to d^3/λ and d^6/λ^4, respectively. These relationships explain in overall terms why the particle size is the main factor of ω (for the conditions spanned by the figure). Particles larger than about 250 µm have a ω close to 1 throughout the mm range. For small particles, the increase of ω as a function of frequency is smaller than expected from the Rayleigh expressions, as there is a counteracting change in n'' (see above).

AMTD
4, 1493–1531, 2011

To better consider real conditions, the mix of different particle sizes must be considered, i.e. the PSD. This has been done in Fig. 3 where the absorption and scattering coefficients have been summed up following the MH97 PSD (Sect. 2.3) and the bulk ω has been calculated. A more detailed analysis reveals that, for MH97, the contribution to the absorption term peaks for particles around 50 µm, while scattering peaks in the 150–300 µm size range (Wu et al., 2005; Eriksson et al., 2008). MH97 achieves a higher IWC primarily by increasing the number of particles larger than about 100 µm. Accordingly, ω is found to monotonically increase with IWC in Fig. 3.

3.3 Source terms

In principle, there is a single source to the measured radiance, thermal emission originating inside the atmosphere. Cosmic background radiation, solar radiation and surface emission give in general negligible or only small contributions. However, both with respect to physical and simulation aspects there is a large difference if the radiation is emitted directly or is scattered into the line-of-sight, and it makes sense to also separate the source into two terms: emission and scattering.

The emission is directly linked to absorption as long as local thermodynamic equilibrium (LTE) applies, which is implied by Eqs. (1) and (8). The emission generated along a small path segment Δl is $aB\Delta l$.

The scattering into the line-of-sight for the same segment is $sS\Delta l$. That is, both the emission and scattering source terms (aB and sS, respectively) are proportional the corresponding extinction coefficient. (For vector radiative transfer it is, in general, not possible to express the scattering source term as the product of a scattering coefficient and a normalised scattering function, as for the scalar case here.)

As the extinction, the emission source function depends only on the local conditions. Expressed in brightness temperature, the Planck function is $B = T$. The scattering source function, S, behaves completely differently, it depends both on the scattering function (p) and non-local conditions though the incoming radiation field (Eq. 11). Figure 1 exemplifies S for the case of small particles and weak scattering.

AMTD
4, 1493–1531, 2011

3.4 Discussion

A straightforward test of the importance of ice particle absorption is to repeat some simulations with the scattering quantities set to zero. Results from such a test are found in Fig. 4. The simulations were performed with vector radiative transfer, but the results can be understood in the scalar framework.

Let us first assume that scattering dominates totally, which is the general assumption that is challenged. In this case, Eq. (8) can be written as ($k = s$)

$$\frac{\mathrm{d}I}{\mathrm{d}l} = s(S - I). \tag{12}$$

This equation shows that a fixed scattering coefficient s gets its maximum impact when there is a large difference between I and S. The case of $I \gg S$ is for longwave radiation only encountered when the observation direction is directly towards the sun and is not relevant here. The other extreme situation is $I = 0$.

Equation (12) explains why ΔI in Fig. 4 for 4 and 14 km tangent altitude has opposite sign. For 14 km, the clear-sky I is about 50 K, while S is in the order of 130 K (Fig. 1). Thus, $S > I$ and scattering increases the measured intensity; the source term exceeds the extinction. The situation for 4 km is reversed. The extinction acts here on radiation originating from the lower troposphere and $I > S$ and the impact of clouds is a decrease in observed radiance.

This difference between "low" and "high" tangent altitudes is well-known (Emde et al., 2004b; Wu et al., 2005; Ekström et al., 2007). This study deals primarily with the "high" case. The "low" case is basically parallel to the down-looking geometry considered for dedicated cloud ice sensors (Evans et al., 2002; Buehler, 2007). The transition from positive to negative change in I due to cloud scattering depends on the position of the particles with respect to the tangent point, but occurs roughly at (the highest) altitude where the green and red lines in Fig. 1 cross.

AMTD
4, 1493–1531, 2011

Reversely, if scattering can be neglected:

$$\frac{\mathrm{d}I}{\mathrm{d}l} = a(B - I). \tag{13}$$

Equations (12) and (13) follow the same pattern, but the fact that in general $B > S$ causes important differences. If we here start with the 4 km tangent altitude, I is just slightly larger than B; the absorbed part is replaced with emission of more or less the same power. This explains why ΔI_{abs} is close to zero for the 4 km data in Fig. 4.

For 14 km, we have a parallel situation to the scattering part. However, $B - I$ is roughly double as high as $S - I$ (assuming the conditions of Fig. 1) and some absorption extinction gives a higher $\mathrm{d}I/\mathrm{d}l$ than scattering of same strength ($a = s$). This was pointed out in Eriksson et al. (2008), but not explained in any detail.

Figure 4 shows this in practice, where on average ΔI_{abs} is about 25% of ΔI despite that for most cases $\omega > 0.8$ (Fig. 3). The varying distance to 1-to-1 line is caused by multiple-scattering effects, and the fact that some cases have widespread clouds with low IWC, and then relatively low ω, while other are more compact with high IWC and ω.

If $I = S$, scattering gives no net effect ($\mathrm{d}I/\mathrm{d}l = 0$). If $B > S$ for the same position there is a net contribution through the absorption coefficient. Hence, at positions with these conditions, the ice particles effectively act as $\omega = 0$ independently of the actual ω. This small example shows that single scattering albedo only gives partial information on the relative importance of absorption and scattering for measurements of atmospheric emission. For "low" tangent altitudes, the effective ω is throughout close to 1. On the other hand, for "high" tangent altitudes, ω gives an underestimation of the contribution of particle emission.

4 Polarisation

Figures 5 and 6 show the simulation results used in this section. The optical depths are calculated by propagating a unit Stokes vector ($[1,0,0,0]^T$) through the atmosphere

AMTD
4, 1493–1531, 2011

considering only extinction, and taking $\tau^I = -\log(I)$. The cloud optical depth is obtained by removing τ of the corresponding clear-sky calculation.

The cloud induced change of the intensity is, for the 14 km tangent altitude, strictly positive (Fig. 5), in line with the "high" case discussed in Sect. 3.4. As a help to understand the spread of ΔI (for a fixed τ^I), the clear-sky optical thickness is included in Fig. 6. The figure shows that clouds embedded in an atmosphere with higher gaseous absorption give lower ΔI, which is also consistent with Sect. 3.4. Some cases even show the characteristics of the "low" case with negative ΔI.

Further for Fig. 6, high negative ΔI, and negative ΔI for lower clear-sky τ, are an indication of compact clouds, probably extending downwards and associated with deep convection. This situation can reduce the scattering source function to such a degree that $S < I$ also for the 12 km tangent altitude. Clouds with the same optical thickness, but showing a high positive ΔI are likely widespread clouds with relatively low IWC.

4.1 The scattering matrix

The discussion below of polarisation effects is facilitated by a basic view of the properties of the scattering matrix (**Z**). For spherical particles and so called "macroscopically isotropic and symmetric media" they are well-described in textbooks (Mishchenko et al., 2002; Battaglia et al., 2006). The scattering matrix for horizontally aligned aspherical particles, that are assumed here, is more complex.

Surface effects can be neglected for 347.5 GHz, and the radiation field inside the atmosphere without scattering is unpolarised ($[I,0,0,0]^T$). If a single particle is placed in the atmosphere, the radiation scattered into the line-of-sight from each incoming direction is

$$[Z_{11}I, Z_{21}I, Z_{31}I, Z_{41}I]^T, \quad (14)$$

where I is the incoming intensity and Z_{ij} is the element of **Z** for row i and column j. That is, for conditions of single scattering, only the first column of **Z** is of importance. Example values for this column are shown in Fig. 7.

AMTD
4, 1493–1531, 2011

The figure treats scattering from a zenith angle of 100°, to the limb-direction (90°). The absolute values of the azimuth angles do not matter, and the $\hat{\boldsymbol{n}}$-direction is arbitrarily set to be at 0°. The exact backward and forward directions are not covered by the figure (they deviate with 10° in the zenith direction), but they are relatively close compared to the width of the "scattering lobes" and the relative size of Z_{11} at 0° and ±180° shows that this particle has a somewhat stronger forward than backward scattering. This is also expected as the particle has a size parameter of 0.62, thus found in the lower end of the Mie regime. Rayleigh scattering is equally strong in the forward and backward directions.

4.2 *Q*

The magnitude of *Q* is strongly influenced by particle shape and orientation (Czekala, 1998). For a given shape, the value of *Q* is the smallest for randomly oriented particles. A comparison of Figs. 14 and 15 in Emde et al. (2004a) indicates that this orientation also has the most complex variation regarding the sign of *Q*.

For oriented particles, several studies have shown that the size of *Q* depends on the asphericity (e.g. Miao et al., 2003), and this is also seen in Fig. 5. With orientation, the signs of Δ*I* and *Q* appear to be highly correlated (see Fig. 6, Fig. 15 of Emde et al., 2004a, and Fig. 2 of Davis et al., 2005a). To the degree orientation exists, it is expected that the longest dimension is found close to the horizontal plane (e.g. Bréon et al., 2004), as also assumed in the set-up of these simulations. In this case, Δ*I* and *Q* vary in an anti-correlated manner. For "low" tangent altitudes Δ*I* is negative and *Q* positive, and the opposite is valid for "high" altitudes.

More in detail, horizontally aligned oblate spheroids with an aspect ratio above one can be thought of having a greater size parameter in the horizontal direction than vertically (except for zenith angles of 0° and 180° where they are equal). This means that the extinction cross-section will be greater for the horizontally polarised radiation component than for the vertically one. Consequently, for "low" tangent altitudes *Q* is expected to be positive, as extinction dominates the cloud induced signal (Sect. 3.4).

AMTD
4, 1493–1531, 2011

For "high" tangent altitudes ΔI and (thereby also Q) is dominated by contribution from radiation scattered into the line-of-sight. Since the particles have a greater horizontal than vertical scattering cross-section, more horizontal than vertical polarised radiation is scattered into the line-of-sight. This gives that we expect Q to be negative for "high" tangent altitudes.

However, the correlation between ΔI and Q disappears for strong (multiple) scattering. This can be seen in Fig. 5, where the cases with highest τ are mainly found on the negative side for ΔI while Q is centred around zero.

4.3 U

As mentioned in the Introduction, we have not found any study on U and V for microwave limb sounding. An example where U is investigated for down-looking geometry is Adams et al. (2008).

In Figs. 5 and 6, U deviates from zero only marginally for cloud optical thicknesses below 0.1, i.e. weak cloud scattering. Equation (14) gives for these cases a good description of the radiation scattered into the line-of-sight, where the term of concern here is $Z_{31}I$. Figure 7 shows that Z_{31} is asymmetric around the vertical plane through the line-of-sight, while I is expected to have a low variation with azimuth angle. This results in that the azimuthal integral of $Z_{31}I$, for each zenith angle, is close to zero. Hence, the contributions to U from the "left" and "right" hemispheres for incoming radiation are more or less equally large, but have different sign, and the end result is close to zero.

For a given particle size, Z_{31} has a low dependency on the incoming zenith angle (not shown). On the other hand, Z_{31} varies with particle size, where even the sign can change (Fig. 8). This means that small and large particles give counteracting contributions to U. However, the asymmetry around the vertical plane noted above is throughout valid (can be understood by symmetry reasons).

The azimuthal in-dependency of I is violated if the scattering point is surrounded by clouds. The contributions from left and right sides can then deviate significantly and the observed Stokes vector can have a significant U-value. In addition, the incoming

AMTD
4, 1493–1531, 2011

radiation has then also a non-zero Q, which is converted to U by elements of **Z** not covered by Eq. (14).

In summary, a non-zero U is primarily an effect of multiple scattering. This explains why U has no preferred sign, as the cloud structures are random with respect to observation direction. There is no systematic difference between U for the two aspect ratios in Fig. 5. Some caution is needed when estimating the clear-sky influence on U. The atmospheric scenarios exhibit 3-D structures for temperature and the gas constituents, but it is not clear to what extent horizontal variability is correctly modelled (Sect. 2.3).

4.4 *V*

For these simulation conditions V does not reach significant levels. The maximum (absolute) value for V is only 0.035 K, about three orders of magnitude below U. The V-element is a fairly parallel case to U, e.g. Z_{41} and Z_{31} show the same symmetry in Fig. 8. The main difference is that $Z_{41} \ll Z_{31}$ for most particles (up to $\sim 400\,\mu$m in Fig. 8). Also, the switch from positive to negative values in Fig. 8 is found at a smaller size for Z_{41} compared to Z_{31} (around 400 and 600 µm, respectively). This should result in a higher cancellation between contributions from small and large particles for V than for U.

5 Retrieval aspects

The implications of the results above for retrievals are discussed here. It is assumed that gaseous constituents are the main target of the measurements. The data are in this section reported as brightness temperatures for single polarisations, to match the response of real receivers, e.g.:

$$T_B^v = I + Q/2, \tag{15}$$

(cf. Eqs. 2 and 3. The difference to the corresponding clear-sky case is denoted as ΔT_b).

AMTD
4, 1493–1531, 2011

As noted above, inversions involving clouds are still a topic of research, and no actual retrievals are made here. Instead, some basic assumptions are made. It is assumed that clouds can be handled, at least, for single scattering situations. Figures 5 and 6 indicate that the break-point between single and multiple scattering is found around cloud optical thickness of 0.1. This statement is based on the observation that ΔI shows low spread and U is practically zero for $\tau^I < 0.1$. It is further assumed that the measurements cannot provide any constrain for the particle shape.

5.1 Selection of polarisation

One aim of the study is to investigate if it is more beneficial to perform the observations at a specific polarisation. If clouds are neglected in the retrievals, the polarisation should be selected in order to obtain lowest possible impact on the spectra. Considering the anti-correlation between ΔI and Q (and that Q is larger than U and V), it is the vertical polarisation that fulfils this criterion. As explained below, selecting lowest ΔT_b, for a given cloud scenario, results in that the cloud extinction is also minimised.

A more elaborated approach is to include clouds in the retrieval process. The main consideration, with respect to the accuracy for gas species, is to obtain best possible estimate of the extinction caused by clouds, in lack of a perfect knowledge on particle shapes. This translates to a demand of a compact relationship between cloud extinction and ΔT_b, over a range of particle aspect ratios. (Size uncertainties are treated in Sect. 5.2.)

Some care is needed in this analysis. The "scalar" optical thickness used in Figs. 5 and 6 (τ^I) should not be used; ΔT_b is better compared to the optical thickness of the clouds for the polarisation of concern (τ^Z, Fig. 9). That is, the extinction of interest is the one acting on the part of the gas emission having the measured polarisation.

For cloud τ^Z below ≈ 0.1 in Fig. 9, there is an equally compact relationship to ΔT_b for all polarisations and aspect ratios. Fits to the data in the lower panel of the figure give basically identical result for all cases. This is not a surprising finding with respect to

AMTD
4, 1493–1531, 2011

the small particles, that are interacting through absorption and emission (totally linked phenomena for LTE).

For larger particles causing scattering, Eq. (12) shows that ΔT_b is also proportional to s (the scattering extinction) as long as the term S is unchanged with particle shape. This is the case for Rayleigh sized particles, as the scattering function of Eq. (11) is not affected by particle shape (nor size) as long as $x \ll 1$. This is not valid for all particles, but, for the limb direction, deviations from the Rayleigh scattering function have relatively small influence. This is the case as the radiation scattered into the line-of-sight can be approximated as step function (see Fig. 3 of Emde et al., 2004a), the up-welling and down-welling parts are each more or less constant with zenith angle (but have different T_b). For limb observations, a change of the scattering function is close to symmetric around the break-point of the step function, and the net effect on S becomes small. This is a simplified treatment of the scattering source term, but the results of Fig. 9 show that it is valid in practise. Another way to express this is that the asymmetry factor (in short, the ratio between forward and backward scattering) is of smaller interest for these measurements. It should be remembered that this symmetry applies only to the limb direction.

The compact relationship to ΔT_b is not found for higher cloud τ^Z, which is a result of multiple scattering. No systematic pattern between the polarisations can be discerned. The conclusion is that all polarisations are equally good with respect to gas species retrievals, and that it should be possible to maintain an acceptable accuracy up to cloud optical thicknesses around 0.1.

However, the possibility of also retrieving cloud properties should not be forgotten. The main aim for observations of this type is to estimate the IWC, and the desired property for these retrievals is smallest possible impact of particle shape on the relationship between particle extinction and IWC.

Figure 10 shows that the vertical and horizontal polarisations lack this feature. This follows from the discussion in Sect. 4.2, explaining that the effective cross-section differs between V and H polarisation, and this difference increases with the aspect ratio.

AMTD
4, 1493–1531, 2011

As a consequence, if e.g. V polarisation is measured, it is not clear if the blue, red or yellow curve shall be used to map cloud extinction to IWC, assuming that the particle asphericity can not be determined by some other mean.

This can also be explained by examining the extinction matrix, that has the structure

$$\mathbf{K}(\theta) = \begin{bmatrix} K_{11}(\theta) & K_{12}(\theta) & 0 & 0 \\ K_{12}(\theta) & K_{11}(\theta) & 0 & 0 \\ 0 & 0 & K_{11}(\theta) & K_{34}(\theta) \\ 0 & 0 & -K_{34}(\theta) & K_{11}(\theta) \end{bmatrix}, \quad (16)$$

where θ is the zenith angle. Thus, the (scalar) extinction coefficient for the vertical component ($[1,1,0,0]^T$) is $K_{11}+K_{12}$, while for the horizontal one ($[1,-1,0,0]^T$) is $K_{11}-K_{12}$. That is, the extinction for V and H differs.

Using the same reasoning, Eq. (16) shows also that the extinction coefficient is the same for the ±45° linear and left/right-hand circular components, and it is K_{11}. This is also the extinction coefficient for total intensity, (if it would have been measured), and I is used as the label in Fig. 10 for the common cloud optical thickness associated with $T_B^{+45^\circ}$, $T_B^{-45^\circ}$, T_B^{lhc} and T_B^{rhc}.

It turns out that the K_{11}-element is weakly affected by the aspect ratio (maintaining a constant volume) for the influential particle sizes, and the curves in Fig. 10 of τ^I for different aspect ratios are close to identical. This gives that the mapping from extinction to IWC for observations of $T_B^{+45^\circ}$, $T_B^{-45^\circ}$, T_B^{lhc} and T_B^{rhc} has a low sensitivity to uncertainties regarding the particle asphericity, and these polarisations obtain here an advantage over the V and H options.

5.2 Representation of particle sizes

Conceptually, the most simple option for the retrievals is to assume a PSD parametrisation, exactly as done for the simulations here. A general parametrisation, such as MH97, could potentially describe average conditions correctly, but the instantaneous

AMTD
4, 1493–1531, 2011

local PSD can deviate strongly. That is, a general relationship between IWC and extinction does not exist. Accordingly, IWC is not a suitable variable to represent the cloud properties and it should be better to instead retrieve the relevant optical properties of the cloud particles.

Each particle type that is introduced in the representation of the optical properties causes an additional calculation cost. Further, the observations provide even in best case just coarse information on the PSD. Thus, the number of variables to describe the particles shall be kept as low as possible. But what is the minimum number of variables required to represent the particle properties?

In Sect. 3 it is shown that particle absorption can not be neglected, and that the source functions associated with emission and scattering differ. Hence, at least two variables are needed to give the retrieval a possibility of fitting effects originating from both absorption and scattering. These effects can in rough terms be assigned to "small" and "large" particles, respectively.

Absorption effects are fully described by the absorption coefficient (a), and a single size is sufficient to represent the impact of the small particles. If this absorption coefficient can be determined, it can be translated to an IWC with high accuracy, as the absorption in Rayleigh domain is proportional to the particle volume (Sect. 3.2).

The results in Sect. 5.1 indicate that an exact representation of the scattering function is not needed, the relationship between cloud scattering extinction and ΔT_b is weakly affected by the particle size. This has the consequence that the effects of scattering can also fairly well be covered by a single particle size. A particle size that gives a single scattering albedo close to 1 should be selected if it is important to maintain a clear distinction to the absorption of the small mode. However, it should be more important to maintain a high similarity between the scattering functions of the particle type applied and the true particle ensemble. This points towards using a particle size around 200 µm, as the product of scattering cross-section and the PSD (assuming MH97) peaks in the range 150–300 µm (Wu et al., 2005; Eriksson et al., 2008).

AMTD
4, 1493–1531, 2011

A representation in terms of different particle sizes is assumed above. The task of the retrieval is then to determine the number density of each particle size. A similar option is to instead operate directly with the optical properties. In terms of Eq. (8), the two retrieval quantities are then the absorption (a) and scattering coefficients (s). The normalised scattering function (p) can either be fixed or given a pre-defined relation to s.

The discussion above assumes that the retrieval can estimate absorption and scattering, at least partly, as independent effects, but to what extent this is possible in practical retrievals is not investigated here. However, the possibility of separating the two effects increases if data from two or more wavelength bands can be combined. For single band retrievals, a high variation of the gaseous absorption over the band should be required. If the effects can not be separated, the clouds have to be covered by a single retrieval variable, with a pre-defined relationship between absorption and scattering, most likely following a PSD parametrisation.

6 Conclusions

Detailed simulations of microwave limb sounding at 347.5 GHz involving ice cloud scattering have been performed. The input to the simulations was generated with care to achieve as realistic simulations as possible. The primary aim of the simulations was to improve the general understanding of absorption and polarisation effects caused by ice clouds. Hence, the purpose was not to provide exact statistics of cloud induced radiance changes. This is anyhow not possible as some input variables have large uncertainties, where particle shape and sizes are the most prominent examples.

A main conclusion is that the measurable impact of particle extinction is not highly dominated by scattering, in contrast to down-looking measurements. This difference is a combination of two points. Firstly, limb sounding gives emphasis to higher altitudes where the ice particles tend to have smaller sizes. This gives a higher relative importance of absorption for the particle extinction. Secondly, there is a higher contrast

AMTD
4, 1493–1531, 2011

between the "radiative background" and emission source term for limb sounding. For down-looking data this contrast is close to zero, any particle absorption is replaced by particle emission of almost the same magnitude and the net effect is small. These aspects are not covered by the single scattering albedo, the standard measure on the ratio between scattering and total extinction.

This conclusion has several practical consequences. A first consideration is the generation of the atmospheric scenarios. The magnitude of scattering at 347.5 GHz is constrained fairly well by the CloudSat data from 94 GHz. This as Rayleigh conditions in general apply for both frequencies and the strength of scattering can be scaled as λ_1^4/λ_2^4. On the other hand, CloudSat gives no information on particle absorption and the magnitude of absorption becomes a consequence of the assumed particle size distribution (PSD). However, PSD parameterisations must be judged as uncertain and the application of a single PSD for all cloud types is anyhow a simplification. This generates a substantial uncertainty for some of the results, such as the exact values for ΔI and relative importance of absorption.

Further, no general relationship between cloud extinction and ΔT_b can be established, it depends on the ratio between particle absorption and scattering. This forces the retrieval to handle the cloud optical properties with at least two variables, and, if the measurements provide the necessary information, retrieve these variables as independent quantities. This in order to both avoid systematic errors for the gas constituents and a correct mapping of the cloud extinction to ice water content.

These simulations confirm earlier results regarding the Q element of the Stokes vector. The difference between the brightness temperature of the vertical and horizontal linear components increases with the aspect ratio of the particles, assuming that they have a tendency for orientation alignment. An azimuthal orientation of the particles would give an impact of particle shape also on the higher Stokes elements, U and V, but this effect has not been studied in lack of useful input for the simulations. For oblate spheroids, or particles with random azimuthal orientation, U and V are instead controlled by azimuthal inhomogeneities in the radiation field. These simulations generate

AMTD
4, 1493–1531, 2011

radiances that are more or less constant with the azimuthal angle in the absence of clouds, and such inhomogeneities are mainly associated with cloud effects already in the radiation to be scattered into the line-of-sight, i.e. multiple scattering. The value of U can be significant, while the maximum value of V obtained here is below 0.035 K. This is explained by lower values of the relevant scattering matrix element for V, and also a higher cancellation of contributions from particles of different size.

The results indicate that single scattering can be assumed for cloud optical thicknesses (τ) below about 0.1. For example, values for U and V deviating from zero is only found above this level. In addition, it is shown that for these conditions of thinner clouds there is a compact relationship between τ and ΔT_b, independent of particle shape and observed polarisation component measured. This in its turn signifies that it should be possible to perform gas species retrievals maintaining a high accuracy for $\tau < 0.1$.

With respect to the retrieval of gas constituents, there is thus a small difference between the polarisation options, but with a slight advantage of measuring the vertical component as the cloud extinction is then minimised. On the other hand, it is shown that observing the V or H components gives a dependency of the particle aspect ratio for the conversion from cloud extinction to ice water content (IWC). As U and V have small values (at least for low τ), using any of the $\pm 45^\circ$ or circular components is basically identical to measure the total intensity. The intensity equals the average of the V and H, and the brightness temperature of this average is much less affected by the particle shape than V and H separately. Hence, for retrievals of IWC, it is preferable to select a polarisation component associated with U or V.

A related aspect is to make use of measurements of the same air volume from two orthogonal polarisations. If both measurements are from an identical position, no additional information is obtained by observing the $\pm 45^\circ$ or circular components, while the combination of the V and H components gives a means for a simple detection of cloud influences and possibly also an estimation of the particle aspect ratio. However, if the two measurements come from two different positions, it is hard to disentangle to

AMTD
4, 1493–1531, 2011

what extent differences in ΔT_b are generated by particle shape effects and changed propagation path through the cloud. In the later case, it should be better to avoid the influence of particle shape by using either the ±45° or circular components, and focus on using the two measurements to improve the spatial resolution of the retrieval. This discussion is directly applicable to the PREMIER mm limb sounder, and this study confirms the initial decision to use ±45° polarisation for the over-lapping beams of this instrument.

Acknowledgements. We thank the ARTS community, and particularly Cory Davis who implemented the Monte Carlo module that we have used for the radiative transfer simulations. The public available CloudSat data were an important part of the study. The work was performed as part of an ESA funded project: PREMIER, Consolidation of Requirements and Synergetic Retrieval Algorithms ("CORSA", ESTEC Contract No. 22848/09/NL/CT).

References

Adams, I. S., Gaiser, P., and Jones, W. L.: Simulation of the Stokes vector in inhomogeneous precipitation, Radio Sci., 43, RS5006, doi:10.1029/2007RS003744, 2008. 1499, 1508

Battaglia, A., Simmer, C., Crewell, S., Czekala, H., Emde, C., Marzano, F., Mishchenko, M., Pardo, J., and Prigent, C.: Emission and scattering by clouds and precipitation, in: Thermal Microwave Radiation: Applications for Remote Sensing, edited by: Mätzler, C., The Institution of Engineering and Technolog, London, UK, 101–233, 2006. 1495, 1506

Bohren, C. F. and Huffman, D. R.: Absorption and scattering of light by small particles, Wiley, New York, USA, 1998. 1497

Bréon, F. and Dubrulle, B.: Horizontally oriented plates in clouds, J. Atmos. Sci., 61, 2888–2898, 2004. 1507

Buehler, S. A. and Eriksson, P.: Absorption lookup tables in the radiative transfer model ARTS, J. Quant. Spectrosc. Radiat. Transfer, in review, 2010. 1499

Buehler, S. A., Eriksson, P., Kuhn, T., von Engeln, A., and Verdes, C.: ARTS, the Atmospheric Radiative Transfer Simulator, J. Quant. Spectrosc. Ra., 91, 65–93, 2005. 1499

Buehler, S. A., Jiménez, C., Evans, K. F., Eriksson, P., Rydberg, B., Heymsfield, A. J., Stubenrauch, C., Lohmann, U., Emde, C., John, V. O., Sreerekha, T. R., and Davis, C. P.: A concept

AMTD
4, 1493–1531, 2011

for a satellite mission to measure cloud ice water path and ice particle size, Q. J. R. Meteorol. Soc., 133, 109–128, 2007. 1504
Chandrasekhar, S.: Radiative transfer, Dover, New York, 1950. 1498
Czekala, H.: Effects of particle shape and orientation on polarized microwave radiation for off-nadir problems, Geophys. Res. Lett., 25, 1669–1672, 1998. 1497, 1507
Davis, C., Emde, C., and Harwood, R.: A 3-D polarized reversed Monte Carlo radiative transfer model for mm and sub-mm passive remote sensing in cloudy atmospheres, IEEE T. Geosci. Remote, 43, 1096–1101, 2005a. 1495, 1497, 1499, 1507
Davis, C. P., Wu, D. L., Emde, C., Jiang, J. H., Cofield, R. E., and Harwood, R. S.: Cirrus induced polarization in 122 GHz Aura Microwave Limb Sounder radiances, Geophys. Res. Lett., 32, L14806, doi:10.1029/2005GL022681, 2005b. 1497, 1501
Davis, C. P., Evans, K. F., Buehler, S. A., Wu, D. L., and Pumphrey, H. C.: 3-D polarised simulations of space-borne passive mm/sub-mm midlatitude cirrus observations: A case study, Atmos. Chem. Phys., 7, 4149–4158, doi:10.5194/acp-7-4149-2007, 2007. 1497, 1499
Ekström, M., Eriksson, P., Rydberg, B., and Murtagh, D. P.: First Odin sub-mm retrievals in the tropical upper troposphere: Humidity and cloud ice signals, Atmos. Chem. Phys., 7, 459–469, doi:10.5194/acp-7-459-2007, 2007. 1504
Ekström, M., Eriksson, P., Read, W. G., Milz, M., and Murtagh, D. P.: Comparison of satellite limb-sounding humidity climatologies of the uppermost tropical troposphere, Atmos. Chem. Phys., 8, 309–320, doi:10.5194/acp-8-309-2008, 2008. 1495
Emde, C., Buehler, S. A., Davis, C., Eriksson, P., Sreerekha, T. R., and Teichmann, C.: A polarized discrete ordinate scattering model for simulations of limb and nadir longwave measurements in 1D/3D spherical atmospheres, J. Geophys. Res., 109(D24), D24207, doi:10.1029/2004JD005140, 2004a. 1495, 1497, 1499, 1507, 1511
Emde, C., Buehler, S. A., Eriksson, P., and Sreerekha, T. R.: The effect of cirrus clouds on limb radiances, J. Atmos. Res., 72, 383–401, 2004b. 1496, 1504
Eriksson, P., Ekström, M., Rydberg, B., and Murtagh, D. P.: First Odin sub-mm retrievals in the tropical upper troposphere: Ice cloud properties, Atmos. Chem. Phys., 7, 471–483, doi:10.5194/acp-7-471-2007, 2007. 1496, 1497, 1499
Eriksson, P., Ekström, M., Rydberg, B., Wu, D. L., Austin, R. T., and Murtagh, D. P.: Comparison between early Odin-SMR, Aura MLS and CloudSat retrievals of cloud ice mass in the upper tropical troposphere, Atmos. Chem. Phys., 8, 1937–1948, doi:10.5194/acp-8-1937-2008, 2008. 1496, 1503, 1505, 1513

AMTD
4, 1493–1531, 2011

Eriksson, P., Buehler, S. A., Davis, C. P., Emde, C., and Lemke, O.: ARTS, the Atmospheric Radiative Transfer Simulator, Version 2, J. Quant. Spectrosc. Radiat. Transfer, accepted, 2011. 1498, 1499

Eriksson, P., Rydberg, B., Johnston, M., Murtagh, D. P., Struthers, H., Ferrachat, S., and Lohmann, U.: Diurnal variations of humidity and ice water content in the tropical upper troposphere, Atmos. Chem. Phys., 10, 11519–11533, doi:10.5194/acp-10-11519-2010, 2010. 1496

ESA: PREMIER, report for assessment, Tech. rep., European Space Agency, http://esamultimedia.esa.int/docs/SP1313-5_PREMIER.pdf, accessed: 1 March 2011, 2008. 1494

Evans, K. F. and Stephens, G. L.: Microwave radiative transfer through clouds composed of realistically shaped ice crystals, Part I, Single scattering properties, J. Atmos. Sci., 52, 2041–2057, 1995a. 1496

Evans, K. F. and Stephens, G. L.: Microwave radiative transfer through clouds composed of realistically shaped ice crystals, Part II, Remote sensing of ice clouds, J. Atmos. Sci., 52, 2058–2072, 1995b. 1496

Evans, K. F., Walter, S. J., Heymsfield, A. J., and McFarquhar, G. M.: Submillimeter-wave cloud ice radiometer: simulations of retrieval algorithm performance, J. Geophys. Res., 107, 2.1–2.21, 2002. 1504

Kikuchi, K., Nishibori, T., Ochiai, S., Ozeki, H., Irimajiri, Y., Kasai, Y., Koike, M., Manabe, T., Mizukoshi, K., Murayama, Y., Nagahama, T., Sano, T., Sato, R., Seta, M., Takahashi, C., Takayanagi, M., Masuko, H., Inatani, J., Suzuki, M., and Shiotani, M.: Overview and early results of the Superconducting Submillimeter-Wave Limb-Emission Sounder (SMILES), J. Geophys. Res., 115, D23306, doi:10.1029/2010JD014379, 2010. 1496

Li, J.-L., Waliser, D. E., Jiang, J., Wu, D. L., Read, W., Waters, J. W., Tompkins, A. M., Donner, L. J., Chern, J.-D., Tao, W.-K., Atlas, R., Gu, Y., Liou, K. N., Genio, A. D., Khairoutdinov, M., and Gettelman, A.: Comparisons of EOS MLS cloud ice measurements with ECMWF analyses and GCM simulations: Initial results, Geophys. Res. Lett., 32, L18710, doi:10.1029/2005GL023788, 2005. 1496

Liebe, H. J., Hufford, G. A., and Cotton, M. G.: Propagation modeling of moist air and suspended water/ice particles at frequencies below 1000 GHz, in: AGARD conference proceedings 542: Atmospheric propagation effects through natural and man-made obscurants for visible to mm-wave radiation, 3.1–3.10, Palma de Mallorca, Spain, 17–20 May 1993, 1993. 1500

AMTD
4, 1493–1531, 2011

Livesey, N. J., Snyder, W. V., Read, W. G., and Wagner, P. A.: Retrieval algorithms for the EOS Microwave Limb Sounder (MLS), IEEE T. Geosci. Remote, 44, 1144–1155, 2006. 1495
McFarquhar, G. M. and Heymsfield, A. J.: Parameterization of tropical cirrus ice crystal size distribution and implications for radiative transfer: Results from CEPEX, J. Atmos. Sci., 54, 2187–2200, 1997. 1499
Miao, J., Johnsen, K.-P., Buehler, S., and Kokhanovsky, A.: The potential of polarization measurements from space at mm and sub-mm wavelengths for determining cirrus cloud parameters, Atmos. Chem. Phys., 3, 39–48, doi:10.5194/acp-3-39-2003, 2003. 1497, 1507
Mishchenko, M. I., Travis, L., and Lacis, A.: Scattering, absorption, and emission of light by small particles, Cambridge University Press, Cambridge, UK, 2002. 1497, 1499, 1506
Murtagh, D., Frisk, U., Merino, F., Ridal, M., Jonsson, A., Stegman, J., Witt, G., Eriksson, P., Jiménez, C., Megie, G., de La Noë, J., Ricaud, P., Baron, P., Pardo, J. R., Hauchcorne, A., Llewellyn, E. J., Degenstein, D. A., Gattinger, R. L., Lloyd, N. D., Evans, W. F. J., McDade, I. C., Haley, C., Sioris, C., von Savigny, C., Solheim, B. H., McConnell, J. C., Strong, K., Richardson, E. H., Leppelmeier, G. W., Kyrölä, E., Auvinen, H., and Oikarinen, L.: An overview of the Odin atmospheric mission, Can. J. Phys., 80, 309–319, 2002. 1495
Okamoto, H., Sato, K., and Hagihara, Y.: Global analysis of ice microphysics from CloudSat and CALIPSO: Incorporation of specular reflection in lidar signals, J. Geophys. Res., 115, D22209, doi:10.1029/2009JD013383, 2010. 1501
Rosenkranz, P. W.: Absorption of microwaves by atmospheric gases, in: Atmospheric remote sensing by microwave radiometry, edited by: Janssen, M. A., John Wiley and Sons, Inc., New York, USA, 37–90, 1993. 1495, 1500
Rosenkranz, P. W.: Water vapor microwave continuum absorption: A comparison of measurements and models, Radio Sci., 33, 919–928, 1998, (correction in 34, 1025, 1999). 1500
Rydberg, B., Eriksson, P., and Buehler, S. A.: Prediction of cloud ice signatures in submillimetre emission spectra by means of ground-based radar and in-situ microphysical data, Q. J. R. Meteorol. Soc., 133, 151–162, 2007. 1499
Rydberg, B., Eriksson, P., Buehler, S. A., and Murtagh, D. P.: Non-Gaussian Bayesian retrieval of tropical upper tropospheric cloud ice and water vapour from Odin-SMR measurements, Atmos. Meas. Tech., 2, 621–637, doi:10.5194/amt-2-621-2009, 2009. 1495, 1499, 1500, 1501
Stephens, G. L., Vane, D. G., Boain, R. J., Mace, G. G., Sassen, K., Wang, Z. E., Illingworth, A. J., O'Connor, E. J., Rossow, W. B., Durden, S. L., Miller, S., Austin, R. T., Benedetti, A.,

AMTD
4, 1493–1531, 2011

and Mitrescu, C.: The CloudSat mission and the A-train – A new dimension of space-based observations of clouds and precipitation, Bull. Amer. Met. Soc., 83, 1771–1790, 2002. 1496
Teichmann, C., Buehler, S. A., and Emde, C.: Understanding the polarization signal of spherical particles for microwave limb radiances, J. Quant. Spectrosc. Ra., 101, 179–190, 2006. 1496
Urban, J., Lautié, N., Le Flochmoën, E., Jiménez, C., Eriksson, P., Dupuy, E., El Amraoui, L., Ekström, M., Frisk, U., Murtagh, D., de La Noë, J., Olberg, M., and Ricaud, P.: Odin/SMR limb observations of stratospheric trace gases: Level 2 Processing of ClO, N_2O, O_3, and HNO_3, J. Geophys. Res., 110, D14307, doi:10.1029/2004JD005741, 2005. 1495
Venema, V., Ament, F., and Simme, C.: A stochastic iterative amplitude adjusted Fourier transform algorithm with improved accuracy, Nonlinear Proc. Geoph., 13, 321–328, 2006. 1499
Warren, S. G. and Brandt, R. E.: Optical constants of ice from the ultraviolet to the microwave: A revised compilation, J. Geophys. Res., 113, D14220, doi:10.1029/2007JD009744, 2008. 1502
Waters, J. W., Froidevaux, L., Harwood, R. S., Jarnot, R. F., Pickett, H. M., Read, W., Siegel, P. H., Cofield, R. E., Filipiak, M. J., Flower, D. A., Holden, J. R., Lau, G. K., Livesey, N. J., Manney, G. L., Pumphrey, H. C., Santee, M. L., Wu, W. L., Cuddy, D. T., Lay, R. R., Loo, M. S., Perun, V. S., Schwartz, M. J., Stek, P., Thurstans, R. P., Boyles, M. A., Chandra, K. M., Chavez, M. C., Chen, G. S., Chudasama, B. V., Dodge, R., Fuller, R. A., Girard, M. A., Jiang, J. H., Jiang, Y. B., Knosp, B. W., LaBelle, R., Lam, J. C., Lee, K. A., Miller, D., Oswald, J. E., Patel, N. C., Pukala, D. M., Quintero, O., Scaff, D. M., Snyder, W. V., Tope, M. C., Wagner, P., and Walch, M. J.: The Earth Observing System Microwave Limb Sounder (EOS MLS) on the Aura satellite, IEEE Trans. Geosci. Remote Sensing, 44, 1075–1092, 2006. 1495
Wu, D. L., Read, W. G., Dessler, A. E., Sherwood, S. C., and Jiang, J. H.: UARS/MLS cloud ice measurements: Implications for H_2O transport near the tropopause, J. Atmos. Sci., 62, 518–530, 2005. 1496, 1503, 1504, 1513
Wu, D. L., Jiang, J. H., and Davis, C. P.: EOS MLS cloud ice measurements and cloudy-sky radiative transfer model, IEEE T. Geosci. Remote, 44, 1156–1165, 2006. 1496

AMTD
4, 1493–1531, 2011

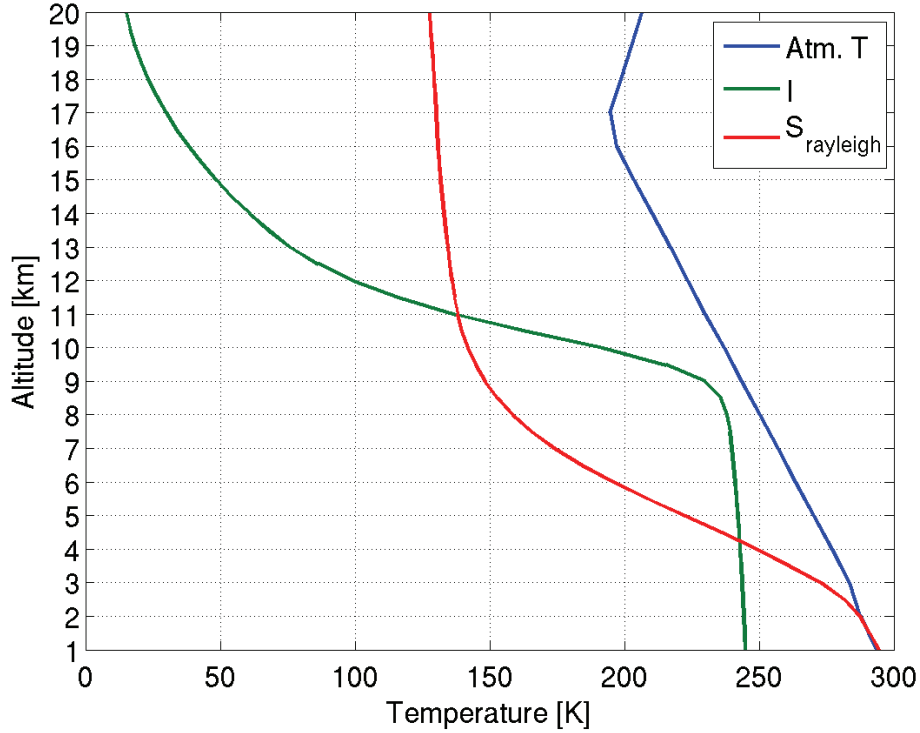

Fig. 1. The atmospheric temperature as a function of altitude (blue), measured *I* is a function of tangent altitude (green), and the scattering source function (S) as a function of altitude (red). The calculation of S assumes single scattering conditions, Rayleigh conditions and a scattering angle of 90° (Eq. 11). The frequency is 347.5 GHz and the data represent average tropical conditions (FASCODE).

AMTD
4, 1493–1531, 2011

On cloud ice induced absorption and polarisation

P. Eriksson and B. Rydberg

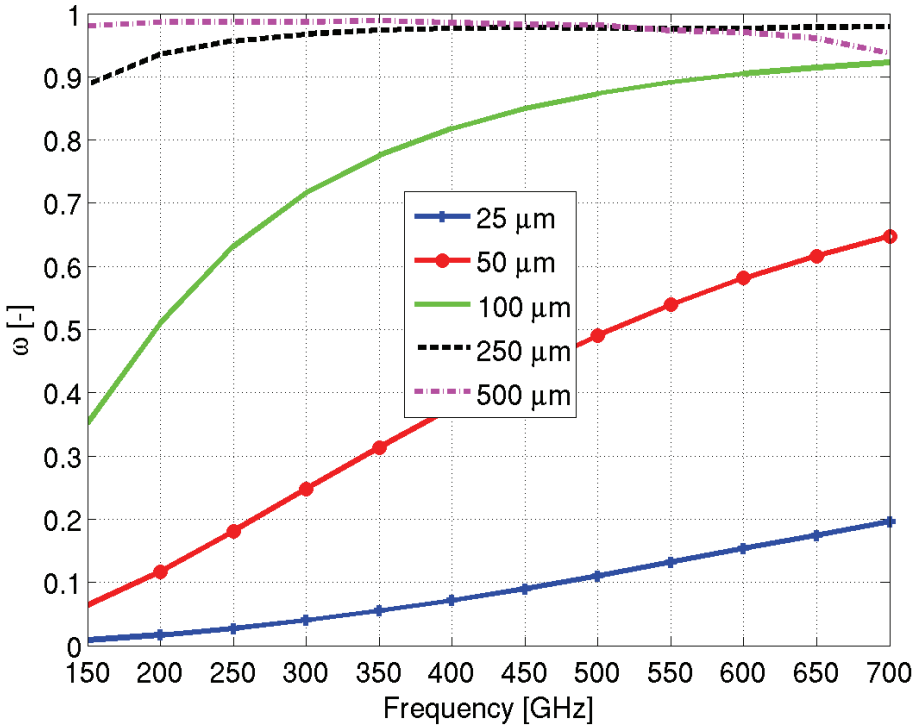

Fig. 2. Single scattering albedo (ω) for five different diameters of spherical ice particles.

AMTD
4, 1493–1531, 2011

On cloud ice induced absorption and polarisation

P. Eriksson and B. Rydberg

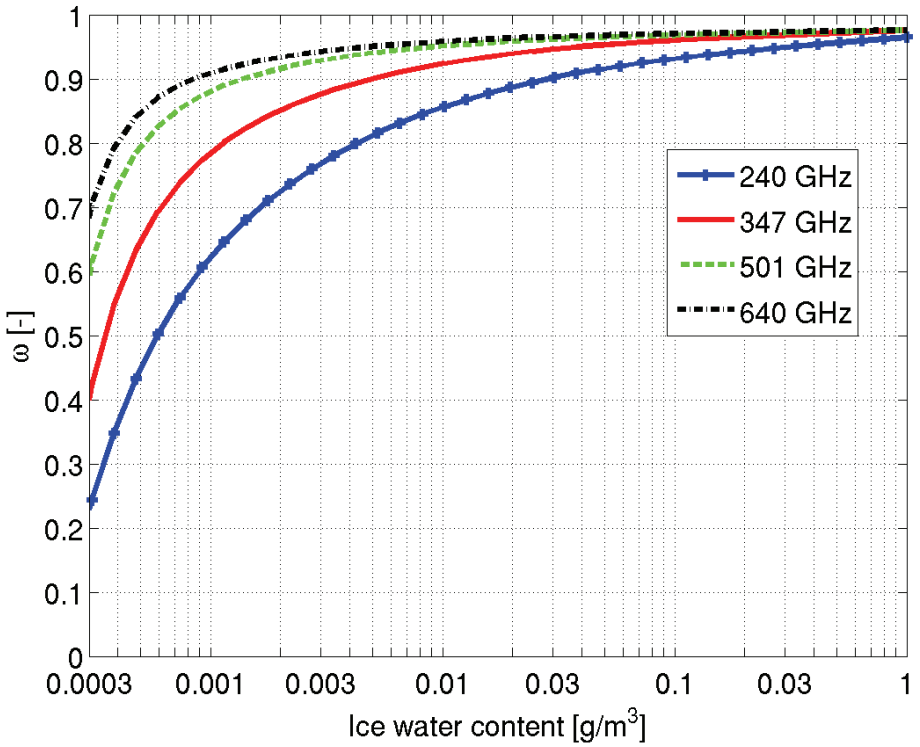

Fig. 3. Single scattering albedo (ω) for spherical ice particles as function of IWC for 4 different frequencies. Particle size distribution according to MH97 for 220 K.

AMTD
4, 1493–1531, 2011

On cloud ice induced absorption and polarisation

P. Eriksson and B. Rydberg

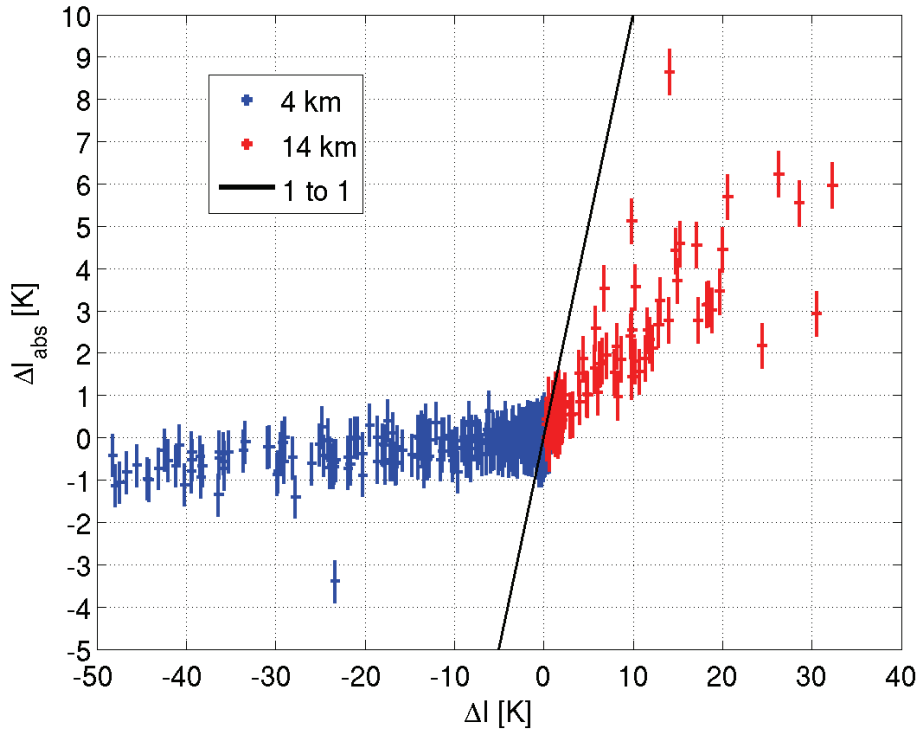

Fig. 4. The ice cloud induced change in intensity for complete simulations (ΔI) and the same when treating the particles as purely absorbing (ΔI_{abs}). The later case was achieved by setting both the scattering matrix and the scattering part of the extinction matrix to zero. The vertical lines show the uncertainty of the scattering calculations ($\pm 2\sigma$), originating from the Monte Carlo approach. Two tangent altitudes were considered, 4 (blue) and 14 (red) km. If scattering would have had a zero contribution, the results would have ended up around the 1 to 1 line (black). The particles were assumed to be horizontally aligned oblate spheroids with an aspect ratio of 2.

AMTD
4, 1493–1531, 2011

On cloud ice induced absorption and polarisation

P. Eriksson and B. Rydberg

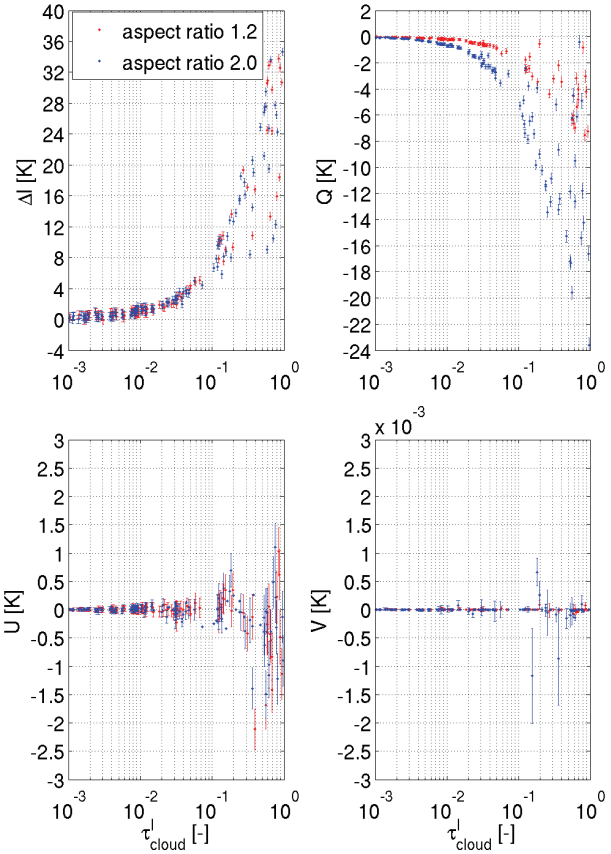

Fig. 5. Simulations of cloud induced change of observed Stokes vector for a collection of atmospheric states, as function of cloud optical depth. The simulations are performed for a frequency of 347.5 GHz and a tangent altitude of 14 km. The ice particles are modelled as horizontally aligned oblate spheroids with an aspect ratio of 1.2 (red) or 2.0 (blue). The vertical lines shows the error estimate ($\pm 2\sigma$) of the Monte Carlo radiative transfer method.

AMTD
4, 1493–1531, 2011

On cloud ice induced absorption and polarisation

P. Eriksson and B. Rydberg

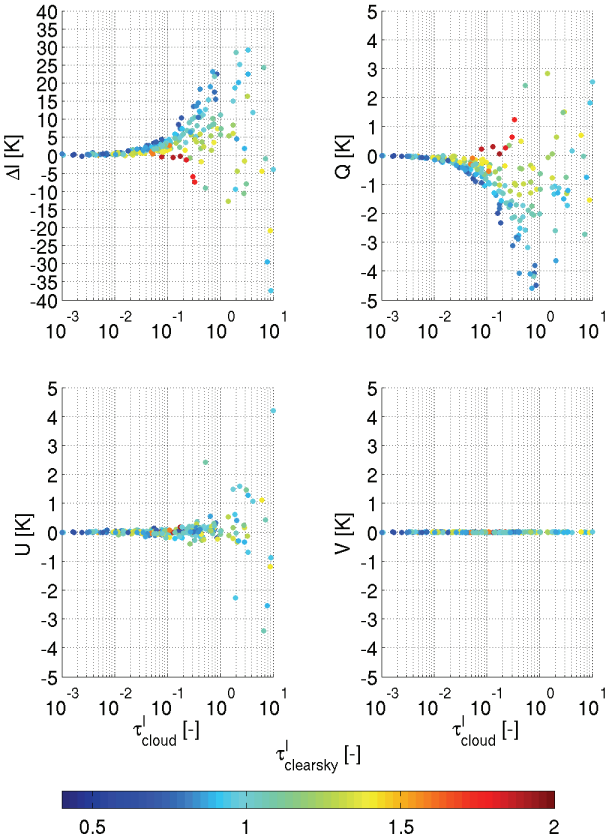

Fig. 6. Simulations of cloud induced change of observed Stokes vector for a collection of atmospheric states, as function of cloud optical depth. The simulations are performed for a frequency of 347.5 GHz and a tangent altitude of 12 km. The ice particles are modelled as horizontally aligned oblate spheroids with an aspect ratio of 1.2. The colours indicate the clear-sky optical depth of the atmosphere (errors are of same size as in Fig. 5).

AMTD
4, 1493–1531, 2011

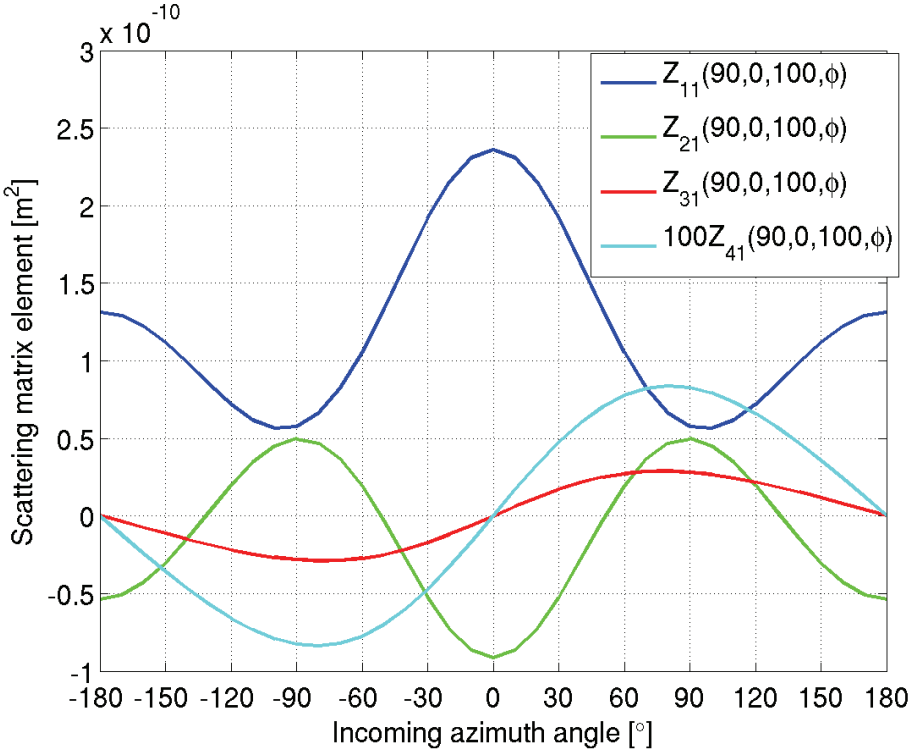

Fig. 7. Scattering matrix elements as a function of incoming azimuth angle, for horizontally aligned oblate spheroids with an aspect ratio of 2, an equivalent diameter size of 170 µm and a frequency of 347.5 GHz. In the nomenclature of Eq. (1), the zenith and azimuth angles of $\hat{\boldsymbol{n}}$ are 90°and 0°, respectively, and the zenith angle of $\hat{\boldsymbol{n}}'$ is 100°. The Z_{41} is increased by a factor of 100, to make the angular variation visible.

AMTD
4, 1493–1531, 2011

On cloud ice induced absorption and polarisation

P. Eriksson and B. Rydberg

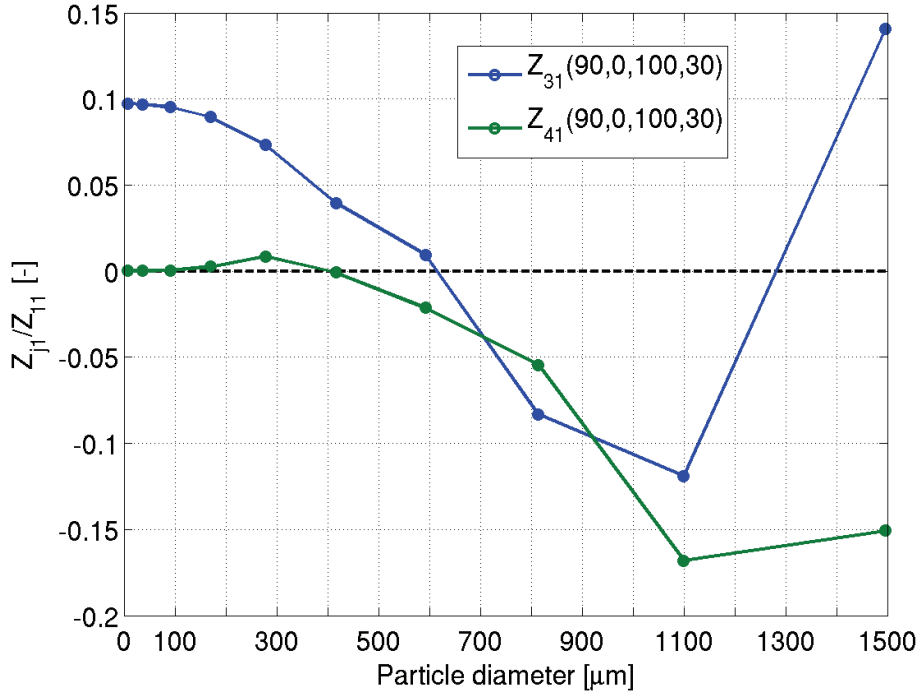

Fig. 8. Normalised scattering matrix elements as a function of particle equivalent diameter for horizontally aligned oblate spheroids with an aspect ratio of 2, and a frequency of 347.5 GHz. In the nomenclature of Eq. (1), the zenith and azimuth angles of $\hat{\boldsymbol{n}}$ are 90°and 0°, respectively, and the zenith and azimuth angles of $\hat{\boldsymbol{n}}'$ is 100°and 30°, respectively.

AMTD
4, 1493–1531, 2011

On cloud ice induced absorption and polarisation

P. Eriksson and B. Rydberg

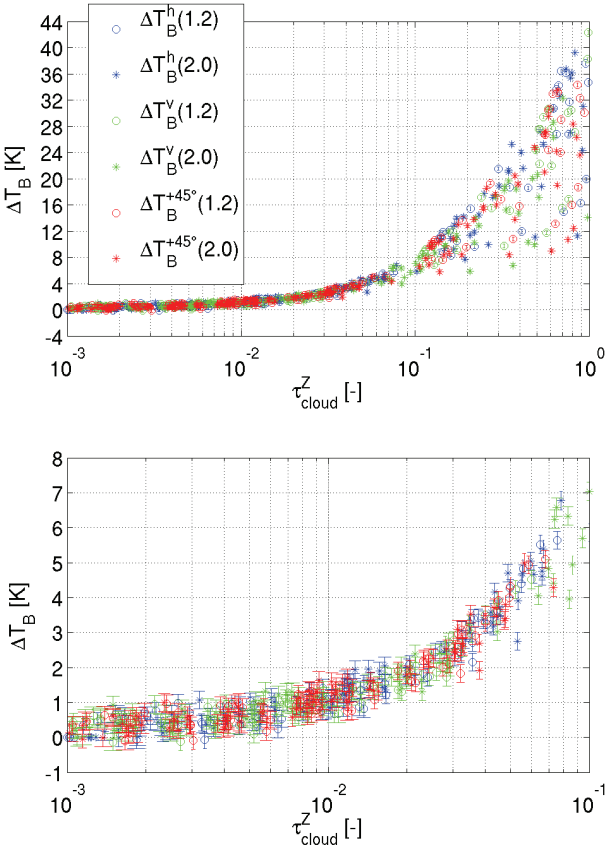

Fig. 9. Simulations of cloud induced signal, as function of polarisation specific cloud optical depth, τ^Z. The lower panel is a magnification of a part of the upper panel. The simulations are performed for a frequency of 347.5 GHz and a tangent altitude of 14 km.

AMTD
4, 1493–1531, 2011

On cloud ice induced absorption and polarisation

P. Eriksson and B. Rydberg

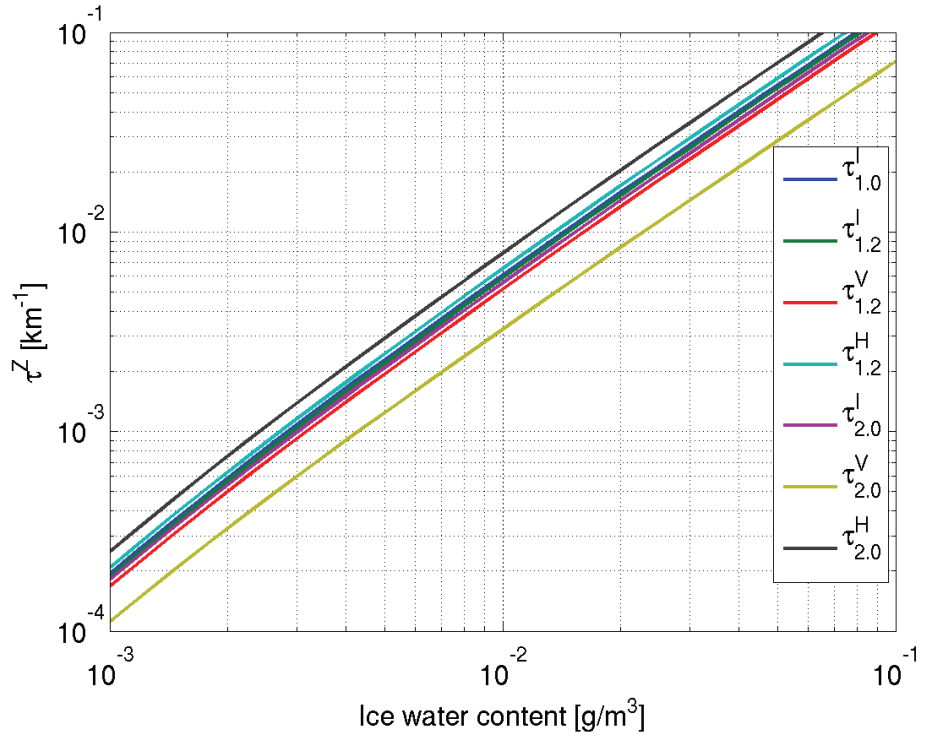

Fig. 10. Cloud ice optical depths for a 90° zenith angle and horizontally aligned oblate spheroids with an aspect ratio of 1, 1.2 and 2.0. Calculated with the PSD of MH97 and a temperature of 220 K. The different lines show the optical depth for different aspect ratios and polarisation components (where / represents several components, as explained in text).

AMTD
4, 1493–1531, 2011

On cloud ice induced absorption and polarisation

P. Eriksson and B. Rydberg